RSC Sustainability

ROYAL SOCIETY OF CHEMISTRY

PAPER

View Article Online
View Journal | View Issue

Cite this: *RSC Sustainability*, 2024, **2**, 3456

Ultra-thin order–disorder CeO_2 nanobelts as the non-carbon support of the PtCu catalyst towards methanol oxidation and oxygen reduction reactions†

Han Zhi,[a] Boda Dong,[a] Xingxing Guo[b] and Feng Xu *[ab]

Received 16th August 2024
Accepted 20th September 2024

DOI: 10.1039/d4su00449c

rsc.li/rscsus

The use of carbon supports in direct methanol fuel cells easily leads to the shedding and poisoning of the Pt catalyst and hence the decrease of catalytic activity. Non-carbon materials have been studied to enhance the metal–support interaction and the catalytic performance. Herein, we explored ultra-thin CeO_2 nanobelts (2D-CeO_2) with the order–disorder structure as the support of the PtCu catalyst. PtCu/2D-CeO_2 shows the highest current density of 37.24 mA cm^{-2} toward the methanol oxidation reaction (MOR), and a limiting current density of 4.82 mA cm^{-2} towards the oxygen reduction reaction. The order–disorder structure of 2D-CeO_2 generates a high volume of oxygen vacancies and strong metal–support interaction. The Pt^0 proportion of PtCu/2D-CeO_2 is much higher than that of PtCu/C which increases the active sites. The d-band center of PtCu is lowered which facilitates the adsorption and dissociation of reactants, thereby dramatically boosting the electro-catalytic performance.

Sustainability spotlight

Direct methanol fuel cells (DMFCs) are widely accepted as one of the promising green energy resources to replace fossil fuels and are now on their way to commercialization. Pt/C is the commonly used catalyst of DMFCs. The carbon support leads to the deactivation during long-term operation. Moreover, carbon is a product of the petrochemical industry. In this work, ultra-thin order–disorder CeO_2 was developed as the non-carbon support to load the PtCu alloy. The results showed better performance towards the methanol oxidation reaction and comparable activity towards the oxygen reduction reaction of PtCu/2D-CeO_2, relative to those of Pt/C. Hence, the activity and durability of Pt-based catalysts were enhanced and the carbon consumption of DMFCs was further cut, promoting the sustainability of our world, aligning with the 7th goal of UN SDG(s), *i.e.*, ensure access to affordable, reliable, sustainable and modern energy for all.

Introduction

To date, platinum supported on carbon (Pt/C) remains the optimum choice as an efficient catalyst in direct methanol fuel cells (DMFCs).[1–3] But Pt suffers from the durability issue and high cost as a noble metal. Both the methanol oxidation reaction (MOR) and oxygen reduction reaction (ORR) have large reaction energy potential barriers, and the reaction rate also shows a serious impact on the overall efficiency.[4] Carbon is a widely used support owing to its high conductivity and specific surface area.[5,6] However, carbon materials are prone to chemical/electrochemical corrosion, which easily leads to the shedding of Pt nanoparticles and the decrease of catalytic activity.[7] Moreover, carbon materials will be oxidized and generate intermediates such as CO*, which poison the Pt catalyst and degrade the overall performance.[8] Therefore, developing novel catalysts to reduce the reaction potential energy barrier and improve the reaction efficiency has become the key issue for DMFCs.[9]

One of the solutions is to explore alternative chemically and electrochemically stable supports which interact strongly with Pt nanoparticles and promote catalytic performance.[10] Researchers have carried out in-depth studies on non-carbon support materials, such as oxides,[11–15] nitrides,[16,17] *etc.* The oxides can effectively alter the electronic structure and prevent the agglomeration of Pt nanoparticles.[18] But the critical drawback of the oxides is the inherent wide band gap which results in poor electron conductivity and severe diminishing of the reaction rate.[19]

It is well known that CeO_2 has the advantage of switching the valence states of cerium ($Ce^{3+} \leftrightarrow Ce^{4+}$), accompanied by charge transfer (including electrons, oxygen anions, and vacancies), which is significantly effective for regulating the ionic/electronic conductivity and the catalytic activity.[20,21] The structure

[a]*School of Advanced Manufacturing, Fuzhou University, Fuzhou, China. E-mail: xufeng@fzu.edu.cn*

[b]*College of Materials Science and Engineering, Fuzhou University, Fuzhou, China*

† Electronic supplementary information (ESI) available. See DOI: https://doi.org/10.1039/d4su00449c

engineering including the morphology, size, facets, and defects is crucial to the regulation. With different nanostructures (nanorods, nanooctahedra, nanocubes, *etc.*), CeO_2 exposes different crystal facets which facilitate certain reactions.[22] The oxygen vacancy of CeO_2 is commonly reckoned critical to tune the interaction with metals and the size of metallic nanoparticles, which are key issues for enhancing the catalytic performance.[23] Amorphous structures have the inherent advantage of abundant vacancies relative to the crystalline counterpart.[24] But amorphous structures suffer from the sluggish kinetics of electron transfer and lower electron conductivity. Therefore, the order–disorder engineering is capable of combining the separate advantages of crystalline and amorphous structures, leading to high catalytic activity.[25] For example, Zhang and co-workers developed amorphous RuO_2 nanosheets with well-defined amorphous-crystalline boundaries supported on carbon cloth, which displayed a low overpotential of 150 mV at 10 mA cm^{-2} and higher durability toward the oxygen evolution reaction.[25]

Herein, we explored ultra-thin two-dimensional CeO_2 nanobelts (2D-CeO_2) with the order–disorder structure as the support of a PtCu alloy to synthesize a dual-function catalyst. 2D-CeO_2 was prepared by the sol–gel method under ambient conditions, and then the PtCu alloy was loaded on 2D-CeO_2. The PtCu/2D-CeO_2 catalysts exhibit better activity and durability than Pt/C towards the MOR.

Experimental section

Chemicals

Chloroplatinic acid hexahydrate ($H_2PtCl_6 \cdot 6H_2O$, analytical grade), copper chloride dihydrate ($CuCl_2 \cdot 2H_2O$, analytical grade), ethylene glycol ($C_2H(OH)_2$, analytical grade), anhydrous ethanol (CH_3CH_2OH, analytical grade), nitric acid (HNO_3, analytical grade), sodium hydroxide (NaOH, analytical grade), sulfuric acid (H_2SO_4, analytical grade), and graphite (C, analytical grade) were all purchased from National Pharmaceutical Reagents. Nafion ($C_{16}H_{33}O$, analytical grade) was purchased from DuPont and deionized water (DI water) was purchased from Aquapro.

Catalyst preparation

Disperse 8.68 g of cerium nitrate hexahydrate ($Ce(NO_3)_3 \cdot 6H_2O$) and 3.2 g of NaOH in 100 mL of deionized water (DI water), and then add the NaOH aqueous solution dropwise to the cerium nitrate aqueous solution. After the droplet addition, the suspension was filtered and washed three times with DI water. After lyophilization, the CeO_2 nanobelts are obtained.

The as-prepared CeO_2 nanobelts were mixed with copper chloride dihydrate ($CuCl_2 \cdot 2H_2O$) in ethylene glycol and the temperature was raised to 185 °C in an oil bath under a N_2 atmosphere and then stirred for 10 min. The product was mixed with an appropriate amount of chloroplatinic acid (H_2PtCl_6) and heated at 60 °C in a water bath for 6 hours, then filtered and lyophilized again. The sample was calcined at 400 °C in a H_2 atmosphere for 2 h. Finally, the calcined sample was stirred in 3 M HNO_3 solution for 12 h to remove the excess Cu that was not alloyed. After filtration and lyophilization, the PtCu/2D-CeO_2 catalyst was obtained. The preparation method of the PtCu/C catalyst was the same as that of the PtCu/2D-CeO_2 catalyst. The difference was that CeO_2 nanobelts were replaced by XC-72 carbon powder. The preparation process of the 25 wt% Pt/C catalyst was the same as the one mentioned above. The specific dosage was 30 mg of XC-72 and 6.64 mL of chloroplatinic acid glycol solution (4 mg mL^{-1}), which was heated in an oil bath at 130 °C for 3 h, and lyophilized to obtain the 25 wt% Pt/C catalyst.

Characterization of the catalysts

The samples were characterized using an X-ray diffractometer (Ultima III X-ray diffractometer), scanning electron microscope (SUPRA 55 Scanning electron microscope), transmission electron microscope (Talos F200i high resolution transmission electron microscope), energy dispersive X-ray diffractometer (EDX), and xseries 2 inductively coupled plasma mass spectrometer.

Electrochemical tests of the catalysts

The catalysts were tested by cyclic voltammetry (CV), linear voltammetry (LSV) and accelerated durability test (ADT) in a conventional three-electrode system. A conventional three-electrode system was used. The working electrodes were the glassy carbon electrode and the rotating ring-disk electrode (5 mm in diameter and 0.196 cm^2 in area), the reference electrode was Ag/AgCl, and the counter electrode was a Pt wire. Electrochemical tests were performed on an Auto Lab electrochemical workstation.

The MOR test was carried out by CV in the potential range of 0.00–1.20 V (*vs.* RHE) with a scanning rate of 50 mV s^{-1}. Before the test, N_2 was bubbled for 30 min to remove the oxygen dissolved in the electrolyte. The CV was then performed in the MOR electrolyte (0.5 M H_2SO_4 + 1 M methanol). The durability was also tested by CV. The ADT cycle was performed in 0.5 M H_2SO_4 solution in the potential range of 0.60–1.20 V (*vs.* RHE). The MOR performance test was conducted once every 1000 cycles to record the MOR performance.

The ORR test was carried out in 1 M $HClO_4$ electrolyte. The LSV test was performed in the potential range of 0.00–1.20 V (*vs.* RHE) at the scan rate of 10 mV s^{-1} and different rotating speeds of 225, 400, 625, 900, 1225, 1600, and 2025 rpm. The durability test was carried out in $HClO_4$ solution. The CV was performed at 0.56–0.96 V (*vs.* RHE) at a scanning rate of 100 mV s^{-1}. A CV in the full potential range was recorded every 1000 cycles, and an ORR catalytic performance test was conducted and recorded after 5000 cycles.

Results and discussion

The prepared 2D-CeO_2 is a two-dimensional energy band structure with a length of about 500 nm and a width of about 100 nm (Fig. 1A). Some fragments with the size under 10 nm are observed. The thickness of 2D-CeO_2 is only several nanometers.

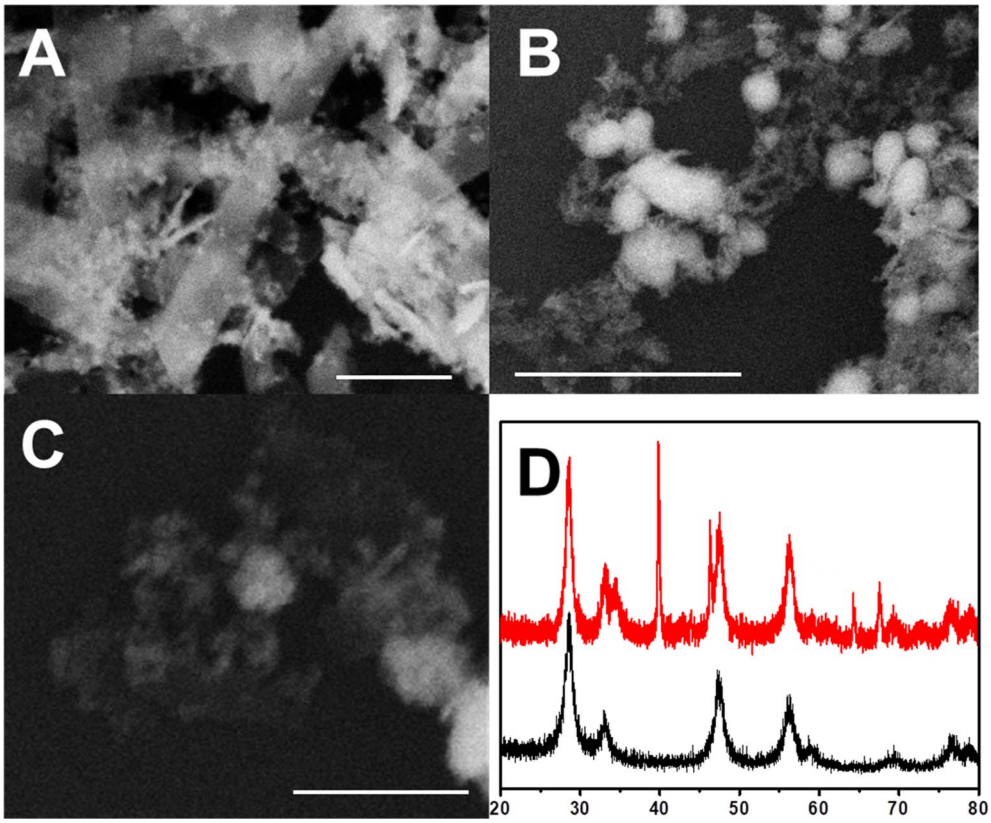

Fig. 1 (A) The SEM images of 2D-CeO_2; (B) 2D-CeO_2 supported Cu; (C) 2D-CeO_2 supported PtCu, and (D) the XRD of PtCu/2D-CeO_2 (red line) and CeO_2 (black line). The scale bars are 100 nm.

The Cu/2D-CeO_2 shows Cu particles with the diameter in the range of twenty to fifty nanometers (Fig. 1B). After Pt displacement and acid leaching, the PtCu particles are intimately loaded on 2D-CeO_2 (Fig. 1C). The XRD illustrates the diffraction signals of PtCu/2D-CeO_2 at 2θ of 28.55°, 33.14°, 47.58°, 56.39°, and 76.70° belonging to the (1 1 1), (2 0 0), (2 2 0), (3 1 1), and (3 3 1) facets of CeO_2 (PDF# 34-0394) respectively (Fig. 1D). Beside the CeO_2 diffraction signals, the sharp peaks at 2θ of 39.76°, 46.24°, 67.45°, and 81.28° are ascribed to the (1 1 1), (2 0 0), (2 2 0), and (3 1 1) facets of the PtCu alloy.[26]

The microstructure of the catalyst was further observed by TEM (Fig. 2). The Cu particles with sizes up to 100 nm can be

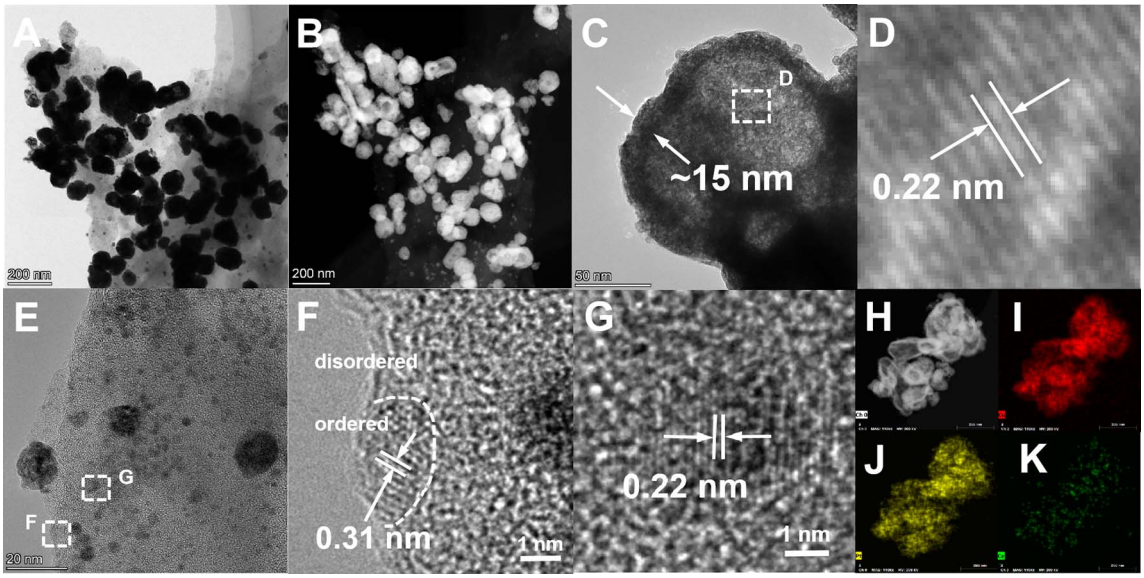

Fig. 2 TEM images of PtCu/2D-CeO_2 (A–G), and high-resolution images (C–G), the EDX element distribution (H–K).

seen (Fig. 2A). The PtCu alloy exhibits two architectures. One is hollow nanospheres with a diameter and wall thickness of about 100 and 15 nm, respectively (Fig. 2B–D). The other is solid PtCu nanoparticles with the size of 2–5 nm (Fig. 2E and F).[27] The lattice spacing value of both architectures is measured to be 0.22 nm, belonging to the PtCu (1 1 1) facet.[28] In the platinum displacement step of the preparation, the reaction is as follows:

$$2Cu + PtCl_6^{2-} \rightarrow 2Cu^{2+} + Pt + 6Cl^- \quad (1)$$

When one Pt atom is reduced, two Cu atoms are oxidized to Cu^{2+} and a defect is formed in the surface of the particle. The defect provides a transport channel through which the internal Cu atoms migrate outward to react with $PtCl_6$.[2–29] With the migration of internal copper ions and the continuous formation of the external PtCu alloy, the hollow nanosphere finally comes into being. This architecture helps expose more active sites, leading to the improvement of catalytic activity.[30]

It is impressive that the 2D-CeO_2 shows two phases, the amorphous and crystalline phases (Fig. 2F). The amorphous phase is the dominant one. The supersaturated nucleation in solution synthesis, because of the low solubility of CeO_2 in water, can construct the amorphous structure.[31] The close observation identifies the crystalline CeO_2 with a size of less than five nanometers. The interplanar spacing value of 0.31 nm, corresponds to the CeO_2 (1 1 1) facet.[32] The well-defined crystalline–amorphous boundary is observed (Fig. 2F). The EDX images show the homogeneous distribution of Pt, Cu, and Ce elements. Therefore, the geometric structure of the catalyst consists of the PtCu nanoparticles and hollow nanospheres homogeneously loaded on the order–disorder 2D-CeO_2.

ICP-AES was used to identify the content ratios of Pt, Cu, and CeO_2 (Table S3†). The mass ratio of CeO_2 is lower than 5%, due to the ultra-thin 2D structure. The Pt loadings of PtCu/2D-CeO_2 and PtCu/C are 75.74 and 82.49 wt% respectively, and the Cu loadings are 19.37 and 17.51 wt% respectively. PtCu/2D-CeO_2 exhibits the Pt : Cu atomic ratio of 1.28, lower than the 1.55 of PtCu/C, revealing that 2D-CeO_2 interacts strongly with Cu and anchors Cu atoms firmly.

XPS was used to analyze the valence and chemical states of the Pt, Cu, and Ce elements (Fig. 3). The peaks at 71.0 and 74.2 eV correspond to Pt^0 $4f_{7/2}$ and Pt^0 $4f_{5/2}$ (Fig. 3A). After splitting, the signals of Pt^0 (p and t), Pt^{2+} (p′ and t′), and Pt^{4+} (p″ and t″) are obtained. Relative to the binding energy (B.E.) of peak p of PtCu/C (71.52 eV), the one of PtCu/2D-CeO_2 (70.97 eV) shifts negatively by 0.55 eV. Through the integrated areas of peaks corresponding to different valence states, the proportion of atoms with different valence states is calculated as follows:

$$Pt^0\% = S_{Pt}{}^0 / (S_{Pt}{}^0 + S_{Pt}{}^{2+} + S_{Pt}{}^{4+}) \times 100\% \quad (2)$$

The Pt^0 proportion (Pt^0%) of PtCu/2D-CeO_2 is 89.34%, much higher than 32.83% of PtCu/C, which indicates the impressive inhibition on the oxidation of the PtCu alloy, due to the Ce^{3+}/Ce^{4+} pairs in CeO_2 which can flexibly adjust their valence states.[33]

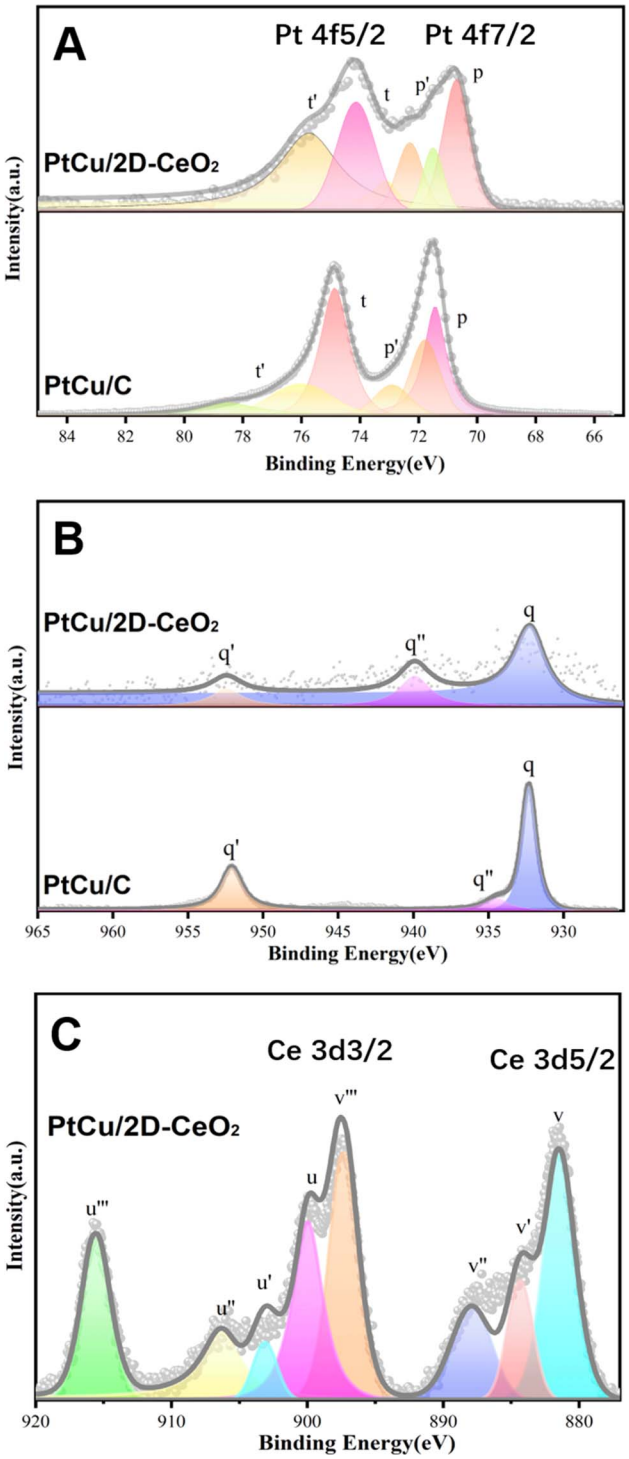

Fig. 3 XPS spectra of Pt 4f (A), Cu 2p (B), and Ce 3d of PtCu/2D-CeO_2 (C) orbitals.

Fig. 3B shows the spectrum of the Cu 2p orbital. The q and q′ peaks represent the Cu^0 $2p_{3/2}$ and Cu^0 $2p_{1/2}$, respectively.[34] Similar to the scenario of the Pt 4f orbital, the Cu^0 peak of PtCu/2D-CeO_2 (931.14 eV) shifts negatively by 1.12 eV relative to the

one of PtCu/C (932.26 eV). The q″ peak corresponding to Cu^{2+} $2p_{3/2}$ is located at 934.8 eV, representing the presence of non-zero valence copper atoms on the catalyst surface, due to the oxygenation of surficial Cu atoms during the catalyst preparation and preservation.[35] The negative B. E. shifts of Pt 4f and Cu 2p orbitals of PtCu/2D-CeO_2 indicate the lower d-band center of the PtCu alloy.[36]

The Ce 3d spectrum shows the peaks at near 882.1 and 902.5 eV representing Ce $3d_{2/3}$ (labeled series c) and Ce $3d_{2/5}$ (labeled series e), respectively. The v, v″, u, and u′ are the characteristic peaks of Ce^{3+}, and the other peaks (v′, v″, v‴, u″, and u‴) corresponded to the characteristic peaks of Ce^{4+}. The presence of Ce^{3+} indicates the existence of oxygen vacancy defects in 2D-CeO_2. The Ce^{3+} proportion in CeO_2 preliminarily determines the concentration of oxygen vacancies. The Ce^{3+} proportion (Ce^{3+}%) is determined by comparing the integral of the characteristic peak of Ce^{3+} with the integral of the full peak as follows:[37]

$$Ce^{3+}\% = \Sigma S_{Ce}{}^{3+}/(\Sigma S_{Ce}{}^{3+} + \Sigma S_{Ce}{}^{4+}) \times 100\% \quad (3)$$

The Ce^{3+}% of PtCu/2D-CeO_2 is calculated to be 24.91%. The disordered structure results in the high Ce^{3+}% and the related concentration of oxygen vacancy defects, which is important to the interaction with PtCu nanoparticles and the catalytic activity.[38]

The CV and MOR plots were recorded, shown in Fig. 4. The as-prepared PtCu/2D-CeO_2 catalyst shows electrocatalytic activity comparable to that of Pt/C (Fig. 4A). PtCu/2D-CeO_2 exhibits a larger thickness of the double-layer in the potential range of 0.4–0.6 V *vs.* RHE, owing to the large surface of CeO_2 nanobelts which can adsorb quantity charge, illustrating that CeO_2 nanobelts possess high conductivity.[39] The electrochemical active surface area (ECSA) diagram was drawn by integrating the hydrogen region in the potential range of 0–0.4 V (Fig. 4B). The ECSA of PtCu/2D-CeO_2, PtCu/C, and Pt/C is 8.91, 11.39, and 8.36 $m^2\ g_{Pt}{}^{-1}$ respectively. Both PtCu/2D-CeO_2 and PtCu/C exhibit higher ECSA than Pt/C, due to the higher activity of the PtCu alloy than Pt.[40] Better electron conductivity of carbon than CeO_2 leads to a higher ECSA of PtCu/C than PtCu/2D-CeO_2. It is still noteworthy that PtCu/2D-CeO_2 illustrates

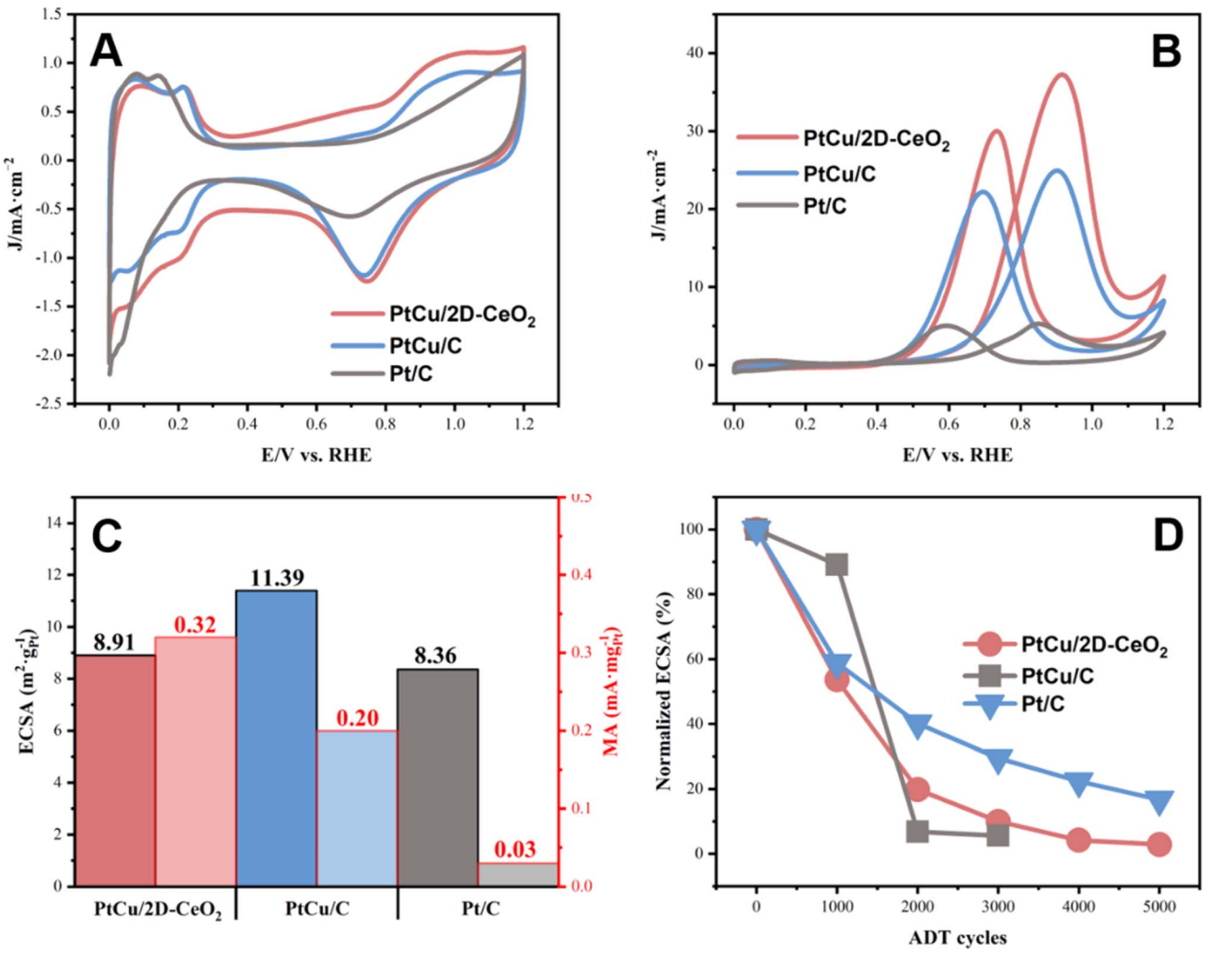

Fig. 4 The CV (A) and MOR (B) plots of PtCu/2D-CeO_2, PtCu/C, and Pt/C; ECSA and MA diagrams of PtCu/2D-CeO_2, PtCu/C, and Pt/C (C); the normalized ECSA after ADT cycling (D).

higher ECSA than Pt/C, revealing higher electrochemical activity. Two factors are crucial to the high activity: (i) the sufficient active sites on which the CH_3OH molecule adsorbs and dissociates, (ii) the high conductivity of the support due to which the electrons coming from the CH_3OH dissociation can be transported to the circuit.[41] The PtCu alloy provides abundant active sites owing to the structure of porous and hollow nanospheres. Moreover, the high Pt^0% as calculated by XPS

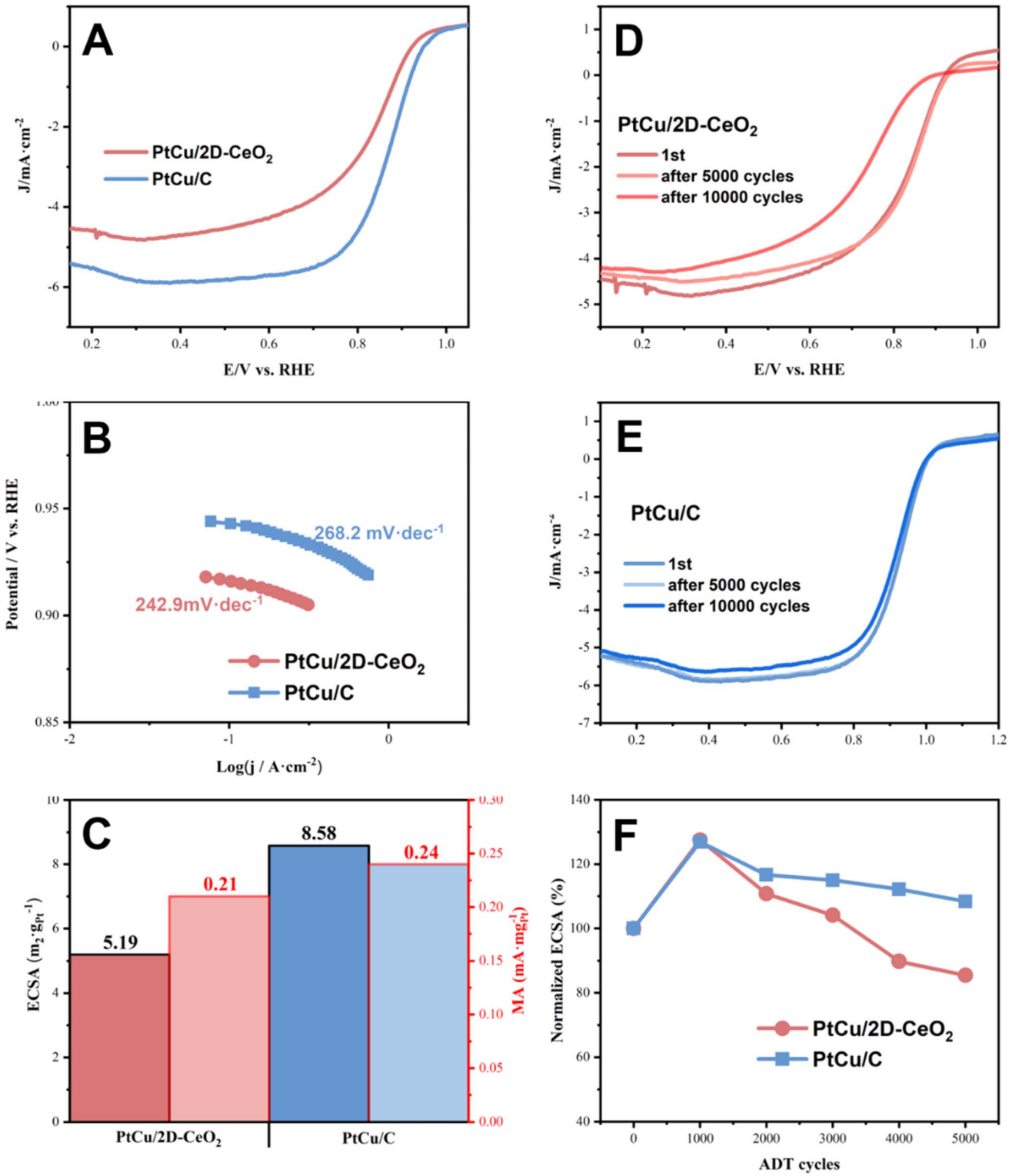

Fig. 5 The LSV curves (A), Tafel slopes (B), and ECSA and MA (C) of PtCu/C and PtCu/2D-CeO_2; LSV curves of PtCu/2D-CeO_2 (D) and PtCu/C (E) 10 000 ADT cycles; and normalized ECSA (F).

represents abundant active sites exposed for reactant adsorption, resulting in the high ECSA.[42] The electron can be transported through oxygen vacancies, and hence, a high volume of oxygen vacancies facilitates electron transportation, leading to the high conductivity.[43] It has been revealed that the 2D materials with the thickness of several nanometers can boost the charge transfer between the support and metal, which promotes the catalytic activity.[44]

Fig. 4B shows the MOR performance of the catalysts. The peak current densities of forward scanning of PtCu/2D-CeO_2, PtCu/C, and Pt/C are 37.24, 24.93, and 5.23 mA cm^{-2}, respectively. The value of PtCu/2D-CeO_2 is 7.08 times that of Pt/C, revealing the very high activity toward the MOR. The MA was calculated based on the limiting current density (Fig. 4C). The MA of PtCu/2D-CeO_2, PtCu/C, and Pt/C is 0.32, 0.20, and 0.03 mA mg_{Pt}^{-1} respectively. The MA of PtCu/2D-CeO_2 is 1.6 and 10.67 times those of PtCu/C and Pt/C, respectively. The specific activity (SA) of the catalyst was calculated from ECSA and MA (Table S4†). The SA of PtCu/C (0.18 mA cm^{-2}) is much higher than that of Pt/C (0.04 mA cm^{-2}), confirming the high activity of the PtCu alloy. PtCu/2D-CeO_2 shows the SA of 0.36 mA cm^{-2}, which is double the value of PtCu/C, owing to the high Pt^0%. The current density ratio of peak values of the forward scanning (I_f) to backward scanning (I_b) is related to the Faraday efficiency, *i.e.*, the oxidation capacity of methanol oxidation and its intermediate products. The I_f/I_b ratios of PtCu/2D-CeO_2, PtCu/C, and Pt/C are 1.24, 1.12, and 1.05 respectively. The higher I_f/I_b ratio PtCu/2D-CeO_2 exhibits better oxidation capability for the intermediates.[45] The durability is also an important issue. Fig. 4D shows the MOR curves of PtCu/2D-CeO_2, PtCu/C, and Pt/C after 5000 cycles and their MA losses. The forward scan current of Pt/C after 1000 cycles was already lower than the negative scanning current value, which indicated that the Faraday efficiency of Pt/C decreased dramatically after 1000 cycles. However the forward scan current of PtCu/C and PtCu/2D-CeO_2 is always higher than negative ones, illustrating the high Faraday efficiency. The degradation of catalytic activity was directly observed by the MA loss. The activity of the Pt/C catalyst decreases sharply after 2000 ADT cycles. The MA of PtCu/C after 5000 cycles retained 14.21%; due to the better durability of the PtCu alloy, the PtCu/2D-CeO_2 gives a slight improvement in durability. The negative shift of the d-band center of Pt 4f and Cu 2p caused by the strong interaction between PtCu and 2D-CeO_2 represents the lower adsorption energy of the reactant and intermediates, which facilitates the MOR. Due to the unique redox behavior between Ce^{3+} and Ce^{4+}, the dissolved Ce ions could also participate in the radical scavenging reaction, which prevents the chemical degradation of polymeric components in the cell.[46]

The ORR activity was also tested (Fig. 5). The onset potentials of PtCu/2D-CeO_2, and PtCu/C catalysts are very close at around 0.93 V. PtCu/2D-CeO_2 shows lower limiting current density (4.8 mA cm^{-2}) than PtCu/C (6.0 mA cm^{-2}). The Tafel slopes of PtCu/2D-CeO_2 and PtCu/C are 242.90 and 268.20 mV dec^{-1} respectively, and the lower value represents that 2D-CeO_2 is of great help to improve the ORR performance. There are two- and four-electron paths in the ORR. The two-electron path generates H_2O_2 which damages the proton exchange membrane;[47] therefore, it is necessary to calculate the number of transferred electrons in the reaction. The K–L equation was used for the diffusion-restricted region to calculate the number of transferred electrons. The electron transfer number of PtCu/2D-CeO_2 is calculated to be 2.66, indicating that the ORR of PtCu/CeO_2 is more inclined to the four-electron transfer process, while the latter is more inclined to the two-electron reaction. To evaluate the durability of the catalysts, we conducted the accelerated durability tests (ADTs) to test their ORR performance after 10 000 cycles (Fig. 5D–F). In the first 1000 cycles, the ECSA of both PtCu/2D-CeO_2 and PtCu/C increases by over 20%, because the active sites are gradually exposed. The performance decreases as the cycling goes on. After 5000 ADT cycles, PtCu/C (108.35%) retains higher ECSA than PtCu/2D-CeO_2 (85.48%). The onset potentials of PtCu/2D-CeO_2, and PtCu/C remain consistent with the original ones.

Conclusions

In this paper, a catalyst with the geometry of order–disorder two-dimensional ceria nanobelt (2D-CeO_2) supported PtCu nanoparticles and hollow nanospheres was prepared. Owing to the order–disorder structure, the 2D-CeO_2 shows a high concentration of oxygen vacancies, leading to the strong interaction with the PtCu alloy. The Pt^0 proportion of PtCu/2D-CeO_2 is much higher than that of PtCu/C, and both Pt 4f and Cu 2p orbitals shift negatively which indicates the lower d-band center of the PtCu alloy. The PtCu/2D-CeO_2 exhibits specific activity which is 10.67 times that of Pt/C toward the methanol oxidation reaction and comparable activity toward the oxygen reduction reaction. The high performance of PtCu/2D-CeO_2 mainly comes from two aspects: (i) the high volume of oxygen vacancies of 2D-CeO_2 facilitates electron transportation, leading to high conductivity. (ii) The sufficient active sites and the lower d-band center of the PtCu alloy facilitate the adsorption and dissociation of reactants. This work offers an attractive avenue to design order–disorder oxide supports to achieve high performance and long-term durability of catalysts.

Data availability

Data are available on request from the authors. The data that support the findings of this study are available from the corresponding author, Feng Xu, upon reasonable request.

Conflicts of interest

The authors declare no competing financial interest.

Acknowledgements

We gratefully acknowledge the financial support from the Natural Science Foundation of Fujian Province (No. 2022J01089).

References

1 L. Huang, X. Zhang, Q. Wang, Y. Han, Y. Fang and S. Dong, *J. Am. Chem. Soc.*, 2018, **140**, 1142–1147.
2 W. Huang, H. Wang, J. Zhou, J. Wang, P. N. Duchesne, D. Muir, P. Zhang, N. Han, F. Zhao, M. Zeng, J. Zhong, C. Jin, Y. Li, S.-T. Lee and H. Dai, *Nat. Commun.*, 2015, **6**, 10035.
3 Q. Fang, H. Wang, X. Lv, X. Wei, X. Luo, J. Huang, L. Jiao, W. Gu, W. Song and C. Zhu, *ACS Sustain. Chem. Eng.*, 2021, **9**, 13039–13046.
4 J. Wang, B. Zhang, W. Guo, L. Wang, J. Chen, H. Pan and W. Sun, *Adv. Mater.*, 2023, **35**, 2211099.
5 X. Fan, M. Zhao, T. Li, L. Y. Zhang, M. Jing, W. Yuan and C. M. Li, *Nanoscale*, 2021, **13**, 18332–18339.
6 M. Li, F. Yang, J. Chang, A. Schechter and L. Feng, *Acta Phys.-Chim. Sin.*, 2023, 2301005.
7 A. Riese, D. Banham, S. Ye and X. Sun, *J. Electrochem. Soc.*, 2015, **162**, F783–F788.
8 G. Bai, C. Liu, Z. Gao, B. Lu, X. Tong, X. Guo and N. Yang, *Small*, 2019, **15**, 1902951.
9 W. Qiao, L. Yu, J. Chang, F. Yang and L. Feng, *Chin. J. Catal.*, 2023, **51**, 113–123.
10 B. Cai, S. Henning, J. Herranz, T. J. Schmidt and A. Eychmüller, *Adv. Energy Mater.*, 2017, **7**, 1700548.
11 H. C. Song, G. R. Lee, K. Jeon, H. Lee, S. W. Lee, Y. S. Jung and J. Y. Park, *ACS Nano*, 2020, **14**, 8335–8342.
12 A. Kakoria, B. Devi, A. Anand, A. Halder, R. R. Koner and S. Sinha-Ray, *ACS Appl. Nano Mater.*, 2018, **2**, 64–74.
13 F. Ando, T. Gunji, T. Tanabe, I. Fukano, H. D. Abruña, J. Wu, T. Ohsaka and F. Matsumoto, *ACS Catal.*, 2021, **11**, 9317–9332.
14 Z. Yan, W. Wei, J. Xie, S. Meng, X. Lü and J. Zhu, *J. Power Sources*, 2013, **222**, 218–224.
15 K. Sasaki, L. Zhang and R. R. Adzic, *Phys. Chem. Chem. Phys.*, 2008, **10**, 159–167.
16 X. Tian, H. Tang, J. Luo, H. Nan, T. Shu, L. Du, J. Zeng, S. Liao and R. R. Adzic, *ACS Catal.*, 2017, **7**, 3810–3817.
17 Y. Kuang, W. Qiao, S. Wang, F. Yang and L. Feng, *ACS Mater. Lett.*, 2024, **6**, 1722–1731.
18 X. Zheng, P. Li, S. Dou, W. Sun, H. Pan, D. Wang and Y. Li, *Energy Environ. Sci.*, 2021, **14**, 2809–2858.
19 J. Yu, D. Wang, G. Wang, Y. Cui and S. Shi, *Adv. Mater.*, 2022, **35**, 2209210.
20 T. A. Zepeda, R. Ponce-Pérez, A. Solis-Garcia, J. Guerrero-Sanchez, S. Fuentes and S. A. Gomez, *Appl. Catal., B*, 2023, **336**, 122936.
21 W. Chen, J. Xue, Y. Bao and L. Feng, *Chem. Eng. J.*, 2020, **381**, 122752.
22 M. Lykaki, E. Pachatouridou, S. A. C. Carabineiro, E. Iliopoulou, C. Andriopoulou, N. Kallithrakas-Kontos, S. Boghosian and M. Konsolakis, *Appl. Catal., B*, 2018, **230**, 18–28.
23 Y. Zhou, A. Chen, J. Ning and W. Shen, *Chin. J. Catal.*, 2020, **41**, 928–937.
24 B. Lu, R. Dun, W. Wang, J. Huang, J. Wu, Z. Hua and J. Shi, *Appl. Catal., B*, 2024, **342**, 123343.
25 Y. Zhang, Y. Zhang, Z. Zeng and D. Ho, *Mater. Horiz.*, 2023, **10**, 2904–2912.
26 F. Xu, S. Cai, B. Lin, L. Yang, H. Le and S. Mu, *Small*, 2022, e2107387.
27 F. Wang, X. Wang, Z. Guo, J. Yu and H. Zhu, *Energy Fuels*, 2021, **35**, 3368–3375.
28 T. Zou, Y. Wang and F. Xu, *ACS Appl. Mater. Interfaces*, 2023, **15**, 58296–58308.
29 M. Guo, Q. Tu, L. Wang, Y. Tang, H. Song, J. Zhou, Z. Zhang, Y. Wang and C. Liu, *Int. J. Hydrogen Energy*, 2019, **44**, 6886–6895.
30 X. Qiao, J. Jin, H. Fan, Y. Li and S. Liao, *J. Mater. Chem. A*, 2017, **5**, 12354–12360.
31 Z. Guo, Z. Liu and R. Tang, *Mater. Chem. Front.*, 2024, **8**, 1703–1730.
32 N. K. Eswar, V. V. Katkar, P. C. Ramamurthy and G. Madras, *Ind. Eng. Chem. Res.*, 2015, **54**, 8031–8042.
33 A. Chen, X. Yu, Y. Zhou, S. Miao, Y. Li, S. Kuld, J. Sehested, J. Liu, T. Aoki, S. Hong, M. F. Camellone, S. Fabris, J. Ning, C. Jin, C. Yang, A. Nefedov, C. Wöll, Y. Wang and W. Shen, *Nat. Catal.*, 2019, **2**, 334–341.
34 Y. Liu, A. Zhang, L. Xue, H. Zhang, Y. Hao, Y. Wang, J. Wu and S. Zeng, *ACS Appl. Energy Mater.*, 2021, **5**, 604–614.
35 F. Jiang, S. Wang, B. Liu, J. Liu, L. Wang, Y. Xiao, Y. Xu and X. Liu, *ACS Catal.*, 2020, **10**, 11493–11509.
36 M. Jin, Y. Liu, X. Zhang, J. Wang, S. Zhang, G. Wang, Y. Zhang, H. Yin, H. Zhang and H. Zhao, *Appl. Catal., B*, 2021, **298**, 120545.
37 F. Xu, K. Cheng, Y. Yu and S. Mu, *Electrochim. Acta*, 2017, **229**, 253–260.
38 Y. Yu, X. Wang, W. Gao, P. Li, W. Yan, S. Wu, Q. Cui, W. Song and K. Ding, *J. Mater. Chem. A*, 2017, **5**, 6656–6663.
39 B. Feng, Z. U. Khan and W. U. Khan, *Environ. Sci.: Nano*, 2023, **10**, 1163–1176.
40 J. Wang, J. Zhang, G. Liu, C. Ling, B. Chen, J. Huang, X. Liu, B. Li, A.-L. Wang, Z. Hu, M. Zhou, Y. Chen, H. Cheng, J. Liu, Z. Fan, N. Yang, C. Tan, L. Gu, J. Wang and H. Zhang, *Nano Res.*, 2020, **13**, 1970–1975.
41 H. Hu, F. Ding, H. Ding, J. Liu, M. Xiao, Y. Meng and L. Sun, *Adv. Compos. Hybrid Mater.*, 2020, **3**, 498–507.
42 G. W. Sievers, A. W. Jensen, J. Quinson, A. Zana, F. Bizzotto, M. Oezaslan, A. Dworzak, J. J. K. Kirkensgaard, T. E. L. Smitshuysen, S. Kadkhodazadeh, M. Juelsholt, K. M. Ø. Jensen, K. Anklam, H. Wan, J. Schäfer, K. Čépe, M. Escudero-Escribano, J. Rossmeisl, A. Quade, V. Brüser and M. Arenz, *Nat. Mater.*, 2020, **20**, 208–213.
43 Y. Fang, H. Li, Q. Zhang, C. Wang, J. Xu, H. Shen, J. Yang, C. Pan, Y. Zhu, Z. Luo and Y. Guo, *Environ. Sci. Technol.*, 2022, **56**, 3245–3257.
44 K. Zhang, W. Guo, Z. Liang and R. Zou, *Sci. China Chem.*, 2019, **62**, 417–429.
45 L. Zhang, L.-X. Ding, H. Chen, D. Li, S. Wang and H. Wang, *Small*, 2017, **13**, 1604000.
46 K. R. Yoon, J. M. Kim, K. A. Lee, C.-K. Hwang, S. G. Akpe, Y. J. Lee, J. P. Singh, K. H. Chae, S. S. Jang, H. C. Ham and J. Y. Kim, *J. Power Sources*, 2021, **496**, 229798.
47 Y. Duan, Y. Sun, S. Pan, Y. Dai, L. Hao and J. Zou, *ACS Appl. Mater. Interfaces*, 2016, **8**, 33572–33582.